Determination of Radiative Forcing of Saharan Dust Using Combined TOMS and ERBE Data

N. Christina Hsu[1], Jay R. Herman[2], and Clark Weaver[3]

For submission to J. Geophys. Res.

June 16, 1999

[1] Raytheon ITSS, Lanham, Maryland 20706

[2] NASA/ Goddard Space Flight Center, Code 916, Greenbelt, Maryland 20771

[3] SM & A Corporation, Arlington, VA 22180

Abstract. The direct radiative forcing of Saharan dust aerosols has been determined by combining aerosol information derived from Nimbus-7 TOMS with radiation measurements observed at the top of atmosphere (TOA) by NOAA-9 ERBE made during February-July 1985. Cloud parameters and precipitable water derived from the NOAA-9 HIRS2 instrument were used to aid in screening for clouds and water vapor in the analyses. Our results indicate that under "cloud-free" and "dry" conditions there is a good correlation between the ERBE TOA outgoing longwave fluxes and the TOMS aerosol index measurements over both land and ocean in areas under the influence of airborne Saharan dust. The ERBE TOA outgoing shortwave fluxes were also found to correlate well with the dust loading derived from TOMS over ocean. However, the calculated shortwave forcing of Saharan dust aerosols is very weak and noisy over land for the range of solar zenith angle viewed by the NOAA-9 ERBE in 1985. Sensitivity factors of the TOA outgoing fluxes to changes in aerosol index were estimated using a linear regression fit to the ERBE and TOMS measurements. The ratio of the shortwave-to-longwave response to changes in dust loading over the ocean is found to be roughly 2 to 3, but opposite in sign. The monthly averaged "clear-sky" TOA direct forcing of airborne Saharan dust was also calculated by multiplying these sensitivity factors by the TOMS monthly averaged "clear-sky" aerosol index. Both the observational and theoretical analyses indicate that the dust layer height, ambient moisture content as well as the presence of cloud all play an important role in determining the TOA direct radiative forcing due to mineral aerosols.

1. Introduction

Tropospheric aerosols perturb the radiative energy balance by directly reflecting and absorbing solar radiation [Penner et al., 1994]. Houghton et al. [1990] showed that the aerosol forcing of climate is comparable in magnitude to the forcing caused by current anthropogenic greenhouse gases but opposite in sign. The Intergovernmental Panel on Climate Change (IPCC) estimated that the global-mean direct forcing due to anthropogenic sulfate and biomass combustion aerosol ranges from -0.3 to -1.5 Wm^{-2} [IPCC, 1994], while Hansen and Lacis [1990] reported that the calculated forcing due to anthropogenic greenhouse gases is about 2.3 ± 0.25 Wm^{-2}. These results suggest that the aerosol cooling effect may partially counteract the warming contributed by greenhouse gas increases over the past few decades.

Among all of the natural and anthropogenic components of tropospheric aerosols, mineral aerosols (dust) play an important role in climate forcing throughout the entire year. Several recent papers have modeled the direct forcing of such aerosols using compiled optical properties of aerosols from various measurements [Tegen et al., 1996; Sokolik et al., 1998]. However, these studies indicate that there are large uncertainties in the estimation of both shortwave and longwave climate forcing of mineral aerosols. Even the sign of the net forcing is not well determined. A thorough regionally-dependent understanding of the chemical, physical and optical properties of aerosols (e.g. chemical composition, size distribution, particle shape, and refractive index) and their spatial and temporal distributions (e.g. aerosol optical thickness or mass loading) is required before we can accurately evaluate aerosol effects in the climate models.

Since tropospheric dust aerosols have a relatively short lifetime (a few hours to about a week), there are large variations in their temporal and spatial distribution. In order to study their direct and indirect effects on the regional and global-scale energy balance, satellite data are needed to obtain continuous temporal and spatial sampling of both the radiative quantities (such as albedo and fluxes) and aerosol abundance. Radiation measurements from the Earth Radiation Budget Experiment (ERBE) have provided well-calibrated measurements of the radiative quantities. However, there are no channels in these instruments for the detection of aerosols so that the scenes with aerosol contamination can be identified. In order to calculate aerosol radiative forcing, additional sources for their detection must be used.

There have been limited attempts to study the regional radiative forcing based upon a few days of collocated AVHRR and ERBE measurements on NOAA-9 [Ackerman and Chung, 1992; Christopher et al., 1996]. These studies provided valuable information on the satellite estimate of aerosol forcing by airborne dust from sandstorm events in the Saudi Arabian Peninsula and smoke from biomass burning in South America. However, the technique of separating clouds from aerosols in the visible wavelengths is time consuming and cannot be easily done on a routine basis. Also, the separation of the signal due to mineral aerosols from that due to the background terrestrial environment can be difficult, particularly over semi-arid regions [Ackerman and Chung, 1992; Tanre et al., 1992].

In this paper, we use TOMS ultraviolet radiance measurements to detect airborne mineral dust over both land and ocean [Hsu et al., 1996; 1999; Herman et al., 1997; Torres et al., 1998]. We will study the TOA direct radiative forcing of airborne Saharan

dust by combining TOMS, ERBE, and HIRS2 data to separate the aerosol pixels from the clear-sky pixels, and to isolate the aerosol effect on the upward shortwave and longwave fluxes at the top of the atmosphere (TOA). The paper is structured as follows.

- After brief descriptions of the satellite measurements used in the analyses in Section 2.1-2.3, we will demonstrate the impact of airborne Saharan dust on the daily observations of the ERBE TOA outgoing longwave and shortwave fluxes in Section 2.4.
- In Section 3, we describe how we use these daily satellite measurements to estimate the sensitivity of the TOA outgoing flux to changes in dust loading over both land and ocean.
- Calculations of the monthly averaged TOA direct forcing of airborne Saharan dust are discussed in Section 4.
- In Section 5 we estimate the changes of the TOA outgoing longwave and shortwave fluxes per unit aerosol optical thickness for sites where sun-photometer aerosol optical thickness measurements are available.
- We will also compare these satellite-observed values with the calculated values derived from radiative transfer models.
- Conclusions are summarized in Section 6.

dust by combining TOMS, ERBE, and HIRS2 data to separate the aerosol pixels from the clear-sky pixels, and to isolate the aerosol effect on the upward shortwave and longwave fluxes at the top of the atmosphere (TOA). The paper is structured as follows.

- After brief descriptions of the satellite measurements used in the analyses in Section 2.1-2.3, we will demonstrate the impact of airborne Saharan dust on the daily observations of the ERBE TOA outgoing longwave and shortwave fluxes in Section 2.4.
- In Section 3, we describe how we use these daily satellite measurements to estimate the sensitivity of the TOA outgoing flux to changes in dust loading over both land and ocean.
- Calculations of the monthly averaged TOA direct forcing of airborne Saharan dust are discussed in Section 4.
- In Section 5 we estimate the changes of the TOA outgoing longwave and shortwave fluxes per unit aerosol optical thickness for sites where sun-photometer aerosol optical thickness measurements are available.
- We will also compare these satellite-observed values with the calculated values derived from radiative transfer models.
- Conclusions are summarized in Section 6.

2. Satellite observations

2.1 TOMS aerosol measurements

Four different TOMS instruments have provided nearly 20 years of daily global-aerosol measurements since November 1978, with a gap from January 1995 until August 1996. In this study, we use data from Nimbus-7 TOMS (November 1978 to May 1993), that has a footprint size of roughly 50 x 50 km^2 at nadir and 100x200 km^2 furthest off nadir (35 cross-orbit scans). The TOMS aerosol data is given in terms of an aerosol index (AI), determined from the Nimbus-7 TOMS 340 and 380 nm radiances (which have negligible dependence on ozone absorption), and is defined as:

$$AI = -100 \{ \log_{10} [(I_{340}/I_{380})_{meas}] - \log_{10} [(I_{340}/I_{380})_{calc}] \} \quad (1)$$

where I_{meas} is the backscattered radiance measured by TOMS at a given wavelength and I_{calc} is the radiance calculated using a radiative transfer model for a pure Rayleigh atmosphere. Essentially, the AI is a measure of the wavelength dependent change in Rayleigh scattered radiance from aerosol absorption relative to a pure Rayleigh atmosphere. The aerosol index is defined so that positive values generally correspond to UV-absorbing aerosols and negative values to non-absorbing aerosols [Hsu et al., 1996; Herman et al., 1997; Seftor et al., 1997; Torres et al., 1998]. Within the range of aerosol optical depths observed from ground-based sun-photometer instruments under biomass burning and regions covered by African dust [Hsu et al., 1999], the TOMS AI measurements are linearly proportional to the AOT. These results are verified by theoretical calculations [Torres et al., 1998].

Because the reflectance over clouds has only a small wavelength dependence, the TOMS AI measurements using two ultraviolet channels can distinguish between cloud-

filled and aerosol-filled scenes. This technique can also be used to detect absorbing aerosols over arid and semi-arid regions. Unlike the thermal-contrast method using infrared channels, the detection of mineral aerosols by TOMS is not susceptible to water vapor absorption and surface temperature variation. Even in the moist Sahel region during the summer months, the correlation is high between TOMS AI and the ground sun-photometer measured aerosol optical thickness [Hsu et al., 1999]. Using theoretical model simulations, however, Torres et al. [1998] have demonstrated that the TOMS AI depends on not only aerosol optical thickness (AOT), but also single-scattering albedo and aerosol height. Although the height of the Saharan dust layer changes from winter to summer, for a given location the dust-plume heights are usually fairly repeatable on a seasonal basis [Hsu et al., 1999].

2.2 ERBE radiation measurements

ERBE includes shortwave (0.2-5 μm), longwave (5-50 μm), and total radiation (0.2-50 μm) wavelength channels. In order to obtain radiation measurements with the smallest footprint, we use the ERBE scanner data. The footprint size of ERBE scanner measurements is approximately 30 km by 45 km at nadir, which is close to that for Nimbus-7 TOMS.

The details of the inversion algorithm to convert radiance into radiant exitence (flux) at the top of atmosphere are described in Barkstrom et al. [1989], Smith et al. [1986] and Suttles et al. [1991]. These inversion procedures essentially constitute two key elements: scene identification and the use of angular distribution models. Scene identification is an important step in the determination of the radiant exitence at the top of

atmosphere, since selection of spectral correction, anisotropic factors, and angular distribution models are all scene dependent.

In the ERBE inversion algorithm, the surface scene types are classified into five different categories: ocean, land, desert, snow, and coastal. Each surface type is then further categorized into clear, partly cloudy, mostly cloudy, and overcast. In the case of heavy smoke or dust, the ERBE algorithm could misidentify these pixels as partly or mostly cloudy, resulting in errors caused by assuming the wrong limbdarkening and bidirectional reflectance models for the conversion. In this study, we will use the archived ERBE TOA albedo and flux measurements, and assume that the effect of the misclassification on the satellite-estimated aerosol forcing is small.

2.3 HIRS2 cloud and water vapor measurements

To isolate the aerosol effect on the radiative budget, the screening of scenes containing clouds and high water vapor content is important. In our study, information on cloud fraction, cloud-top pressure, surface temperature, and precipitable water was provided by data from the NOAA-9 HIRS2 instrument. TOMS reflectivity data were also used as an additional source for cloud screening. The measurements of cloud parameter and precipitable water used are part of the TOVS Pathfinder Path A data set developed by Susskind et al. [1997]. The fields are gridded on a 1° x 1° latitude-longitude grid. Comparisons of these HIRS products against radiosonde data and ECMWF reanalysis indicate that the quality of the HIRS product is adequate for use in climate studies [Susskind et al., 1997].

2.4 Examples of satellite daily maps

To demonstrate the effect of airborne Saharan dust in the regional radiation budget on a daily basis, examples of the daily observations of ERBE radiant flux and TOMS aerosol loading are shown for the region of interest (which includes the Sahara/Sahel areas and the eastern Atlantic). Plate 1 (top) depicts maps of the daily TOA outgoing longwave fluxes observed by the NOAA-9 ERBE scanner in February 1985, while the corresponding daily composites of aerosol index and reflectivity derived from TOMS are shown in Plate 1 (bottom). Clouds are usually associated with higher reflectivity values, and are represented by the gray color shown in the bottom left color bar.

According to the NCEP reanalysis data for early February 1985, an anticyclone centered near Spain was observed with ridge axes extending to western Africa. On the 500-hPa surface, this anticyclone was sandwiched by a strong deep trough over the north Atlantic and another deep trough centered near Cyprus. This combination created a large pressure gradient and strong surface winds, which lifted dust from sources in West Africa and near Lake Chad. Consequently, intense dust plumes were seen over Mauritania, Western Sahara, Senegal, Mali, and Chad.

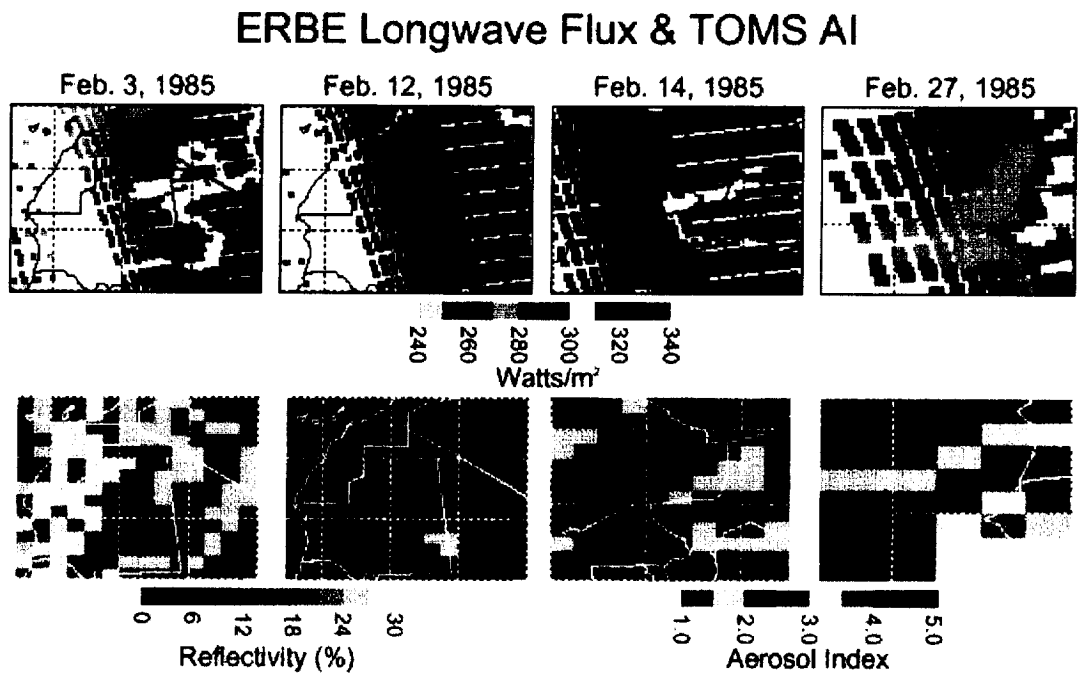

Plate 1 (Top) Maps of the top-of-atmosphere longwave upwelling fluxes observed by the NOAA-9 ERBE scanner in February 1985. The corresponding daily composites of aerosol index and reflectivity derived from TOMS are depicted in Plate 1 (Bottom). Clouds are usually associated with relatively higher reflectivity and are represented by the gray color shown in the bottom left color bar.

The contrast of TOA longwave fluxes between the dust-laden and clear-sky conditions over land is shown by the first two maps (i.e. February 3 and 12) on the top panel. Compared to February 12, the TOA outgoing longwave flux on February 3 decreased by 20-40 W/m^2 in the territories over Mauritania, Mali, and Algeria. These locations are consistent with areas where TOMS, as shown on the bottom panel, detected dust aerosols. More dust storm events were observed over the Sahel region in mid February 1985. On February 14, TOMS detected high dust loading in the region near Niamey, Niger as shown in Plate 1. A reduction in TOA outgoing longwave flux was as much as 10-50 W/m^2 in this area. As dust plumes swept through the continent into the

Atlantic, the aerosol effect on the TOA longwave flux was also observed over ocean. One example, using satellite measurements taken on February 27, shows good correlation between the TOMS observed aerosol distribution and the changes in TOA longwave fluxes over the Atlantic just west of Senegal. The TOA outgoing longwave flux in the eastern Atlantic was reduced from 290-300 W/m^2 to 260-280 W/m^2 on this day.

Plate 2 shows the images of ERBE TOA outgoing shortwave fluxes and the corresponding TOMS aerosol index and reflectivity. The areas included in these images are centered over the Atlantic just west of Africa, since the response of the TOA shortwave fluxes derived by ERBE to changes in dust loading is not clearly seen over land in our analyses. This is consistent with the finding of Ackman and Chung [1992] using ERBE and AVHRR measurements over the Saudi Arabian Peninsula. On February 4, the effect of the dust plume was apparent in the TOA shortwave fluxes in the Atlantic just west of Senegal. There were clouds present in the northwest corner of map, resulting in an increase in the shortwave fluxes in that region.

On average, the TOA outgoing shortwave fluxes increased due to the presence of dust aerosols from approximately 100 W/m^2 to as much as 180 W/m^2. This dust plume continued to move to the west, and on February 6 aerosols were only detected in the upper and left-bottom part of the map. Clouds were also present in the top part of the map. The increase in the TOA shortwave flux observed in the dusty region on this day was about 20 to 80 W/m^2. On February 13, most of the region was dust-free and the values of the TOA shortwave fluxes dropped back to the ocean background level of about 100 W/m^2. On February 27, another intense dust storm occurred near Western Sahara and

Mauritania, resulting in increases of more than 80 W/m^2 in TOA outgoing shortwave fluxes over a vast area of water south of Tenerife and Canary Islands.

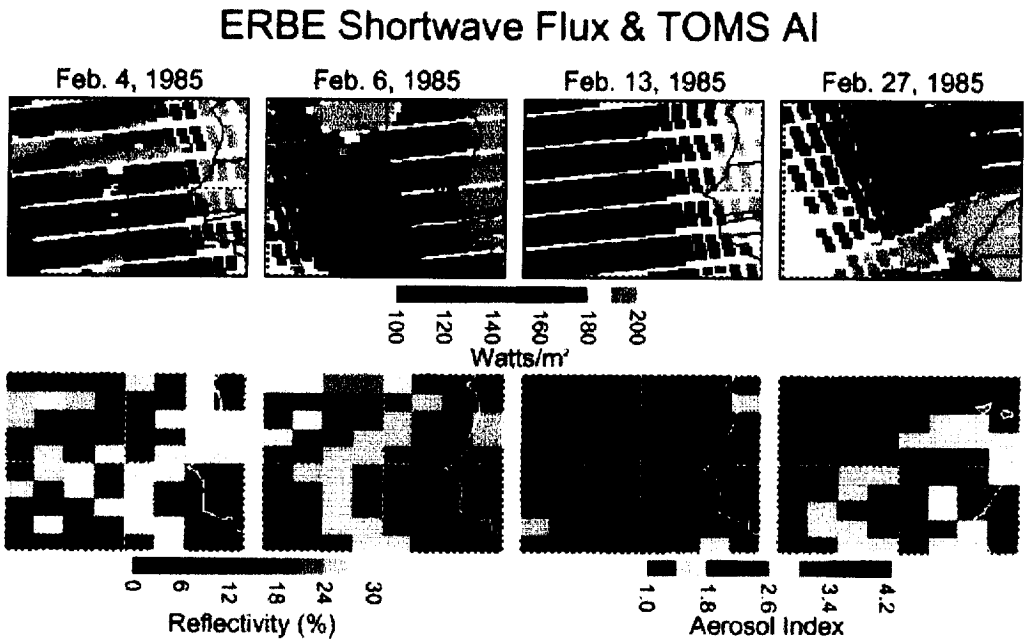

Plate 2 (Top) Similar to Plate 1 (top), except for the top-of-atmosphere shortwave upwelling fluxes. (Bottom) The TOMS aerosol index and reflectivity represented in the similar way as in Plate 1 (bottom). The areas included in these images are centered over the Atlantic just west of Africa.

3. Method and Results

In this section, we discuss how the radiative forcing of mineral aerosols is calculated using the daily satellite measurements described above. The resulting response of TOA radiation due to the presence of mineral aerosols will be shown over both land and ocean. Since both TOMS and ERBE data are snapshot types of measurements taken at near noon and 2:30 p.m., respectively, no time averaging is involved in our estimate of dust radiative forcing. Therefore, the radiative forcing in this study is referred as "direct" or "instantaneous" forcing by aerosols. The Level 2 TOMS aerosol and ERBE flux measurements for the period from February 1985 to July 1985 were binned into 1° x 1° gridded data sets. Since the footprint sizes of both TOMS and ERBE are approximately 45 km by 45 km, the sensitivity to the presence of inhomogeneous subpixel clouds and the underlying ground is roughly the same for both instruments. The combined TOMS/ERBE data were then screened using the 1° x 1° gridded HIRS2 data for the pixels with clouds and water vapor contamination (total precipitable water < 3.5 cm).

Figure 1 (top) shows the plot of the gridded daily ERBE TOA upward longwave fluxes vs. TOMS AI measurements using the method mentioned above for a 2° x 2° box over Africa (29°-31° N; 5°-7° E) for the month of July. It is apparent that there is a good correlation between the TOA outgoing longwave flux and TOMS AI at this location. The linear-regression fit to these data is represented by the solid line with slope and intercept of -9.9 ($\pm$0.9) and 349.8 ($\pm$1.8), respectively. The 1-σ (one standard deviation) errors associated with the regression line coefficients are given in parentheses. The pixels with clouds and high water vapor content were filtered out of the analyses. It is apparent that the ERBE TOA upward longwave fluxes decrease with increasing dust loading.

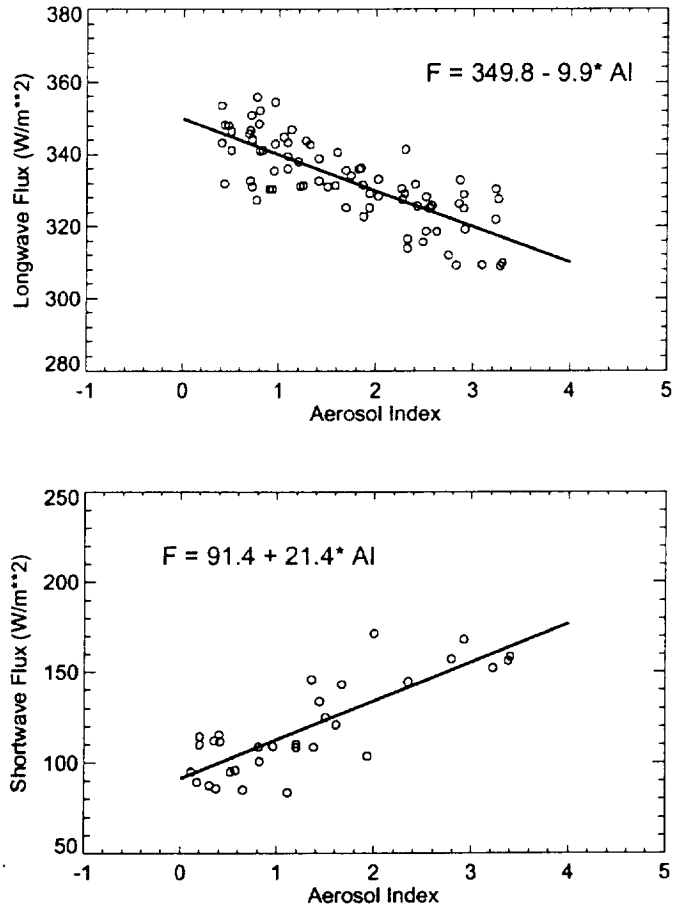

Figure 1 (Top) The relationship of the daily gridded ERBE TOA longwave fluxes and TOMS AI measurements for a 2° x 2° box in Africa (29°-31° N; 5°-7° E) for the month of July. The linear-regression fit to these data is represented by the solid line. (Bottom) The relationship of the daily gridded ERBE TOA shortwave fluxes and the TOMS AI measurements for a 2° x 2° box in the Atlantic (25°-27° N; 19°-21° W) for the month of July.

A similar plot for the ERBE TOA shortwave fluxes vs. TOMS AI data in the Atlantic (25°-27° N; 19°-21° W) is shown in Figure 1 (bottom). The pixels with clouds and high water vapor content were also filtered out of the analyses. The slope and the intercept of the linear-regression line for the shortwave are 21.4 (±2.7) and 91.4 (±4.4), respectively. As seen from this figure, the TOA outgoing shortwave fluxes correlate well

with the TOMS AI over ocean. The ERBE TOA upward shortwave fluxes appear to increase with increasing dust loading.

If we define the dust radiative forcing as the difference between the ERBE flux measured under the dust-laden conditions to that under clear-sky, dust-free conditions, and assume such forcing can be approximated as a simple linear function of the amount of airborne dust, the relationship between the TOA upward flux and dust loading can be expressed as follows:

$$F^{\uparrow TOA} = F_{clear\ sky}^{\uparrow TOA} + sensitivity * AI$$

where $F^{\uparrow TOA}$ denotes the TOA ERBE measured daily flux during daylight and $F_{clear\ sky}^{\uparrow TOA}$ represents the TOA ERBE flux obtained under clear-sky conditions. If statistically significant, the regression line slopes in Figure 1 represent the sensitivity factor of the TOA ERBE flux to changes in aerosol loading and the intercept value is the TOA flux in the dust-free condition. Note that aerosol forcing defined in this fashion is opposite in sign to the quantities usually used by climate models (i.e., $F_{clear\ sky}^{\uparrow TOA} - F^{\uparrow TOA}$). We will apply this regression analysis for each 1° x 1° grid box to calculate the longwave and shortwave sensitivity factors throughout the entire region of interest.

3.1 TOA flux sensitivity to dust loading over land

Figure 2 shows the longwave sensitivity factors, averaged over a 5° latitude band, derived over regions where significant amounts of airborne dust are often observed for February (top) and July (bottom) 1985. Since the maximum dust belt moves northward

from February to July, the February case was represented by the Sahara/ Sahel region (15° to 20° N; 0° to 15° W) and the July case was represented by the Sahara region (29° to 33° N; 5° W to 15° E). For February 1985, the values of the TOA longwave sensitivity to airborne dust over land are around -16±4 W/m^2 per unit AI. These values were found to be fairly consistent throughout the Sahara/Sahel region during February, except for the region near equatorial Africa where low values of longwave sensitivity were observed. These low values over the equatorial forests are most likely due to the effect of smoke generated from biomass burning that often occurs in this region during February.

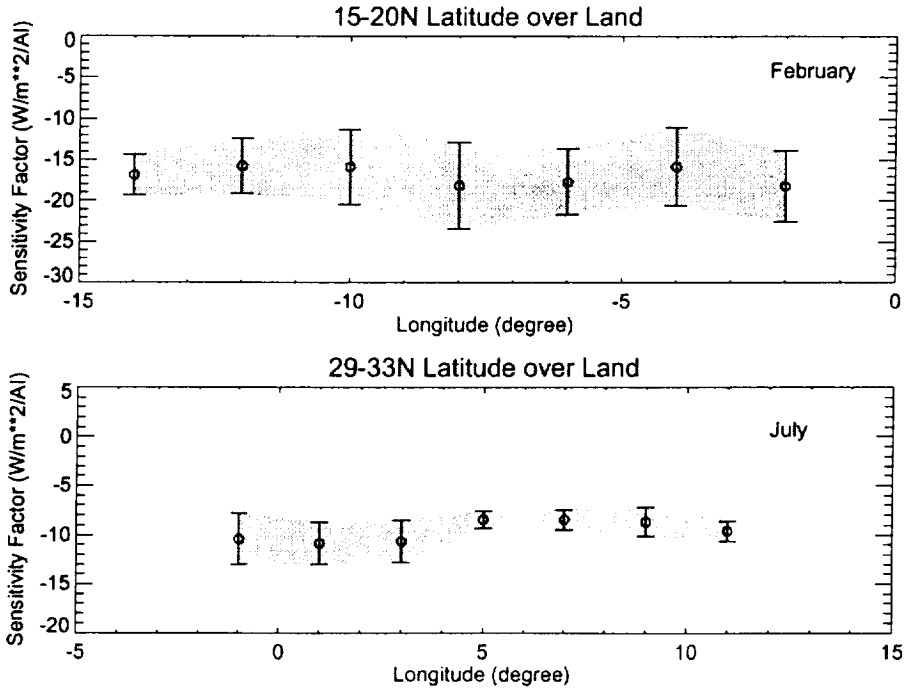

Figure 2. Values of the longwave sensitivity factor derived over land as a function of longitude. The sensitivity factors derived for each 1° x 1° grid box were averaged over a 5° latitude band for 15° – 20° N during February (top), and 29° – 33° N during July (bottom). Circles represent the mean values and bars denote 1-σ of the sensitivity factors derived within the latitude band.

The values of longwave sensitivity factors for July 1985 are approximately -9±1.5 W/m^2 per unit AI over land as shown in Figure 2 (bottom). These values are commonly found in the entire region north of 20° N, except in the mountain areas where higher values are obtained. The correlation of high sensitivity factor and terrain pressure could be due to artifacts associated with algorithms over high-altitude terrain. For the region south of 20° N in July, there are not enough data points that pass the screening of low precipitable water (<3.5 cm) to conduct a regression analysis. If only a cloud screening is applied in our analysis, regardless of the water vapor content, the change in longwave radiation caused by dust storms is found to be very small in the Sahel (south of 17° N) in July. This could be due to cancellation between the effect of airborne dust and water vapor during dust storm events.

Figure 3 depicts the seasonal variations (February to July 1985) of total precipitable water from HIRS2 measurements for the southern zone (15°-20° N; 5°-10° W) and the northern zone (27°-32° N; 5°-10° W). Because the Intertropical Convergence Zone (ITCZ) is near its southernmost position in February, the water vapor content is generally low north of 10° N in the region of interest. Thus, the analyses of the sensitivity factor are less susceptible to problems arising from water vapor contamination. However, as the position of the ITCZ moves northward from winter to summer, the corresponding water vapor content becomes significantly higher in the southern zone (15°-20° N; 5°-10° W) in July compared to that in February. The total precipitable water increases slightly in the northern zone from February to July, producing a strong north-south gradient in the total precipitable water from 15° N to 30° N during July.

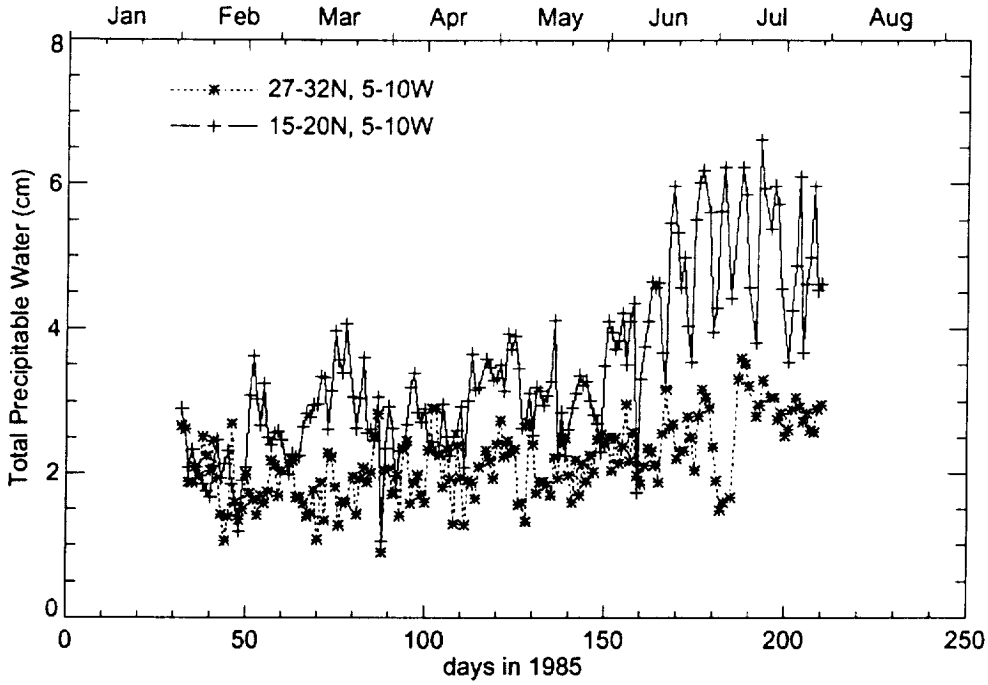

Figure 3. The seasonal variations (February to July 1985) of total precipitable water from HIRS2 measurements for the south zone (15°-20° N, 5°-10° W) (+ symbols) and the north zone (27°-32° N, 5°-10° W) (* symbols). Because the position of the ITCZ moves northward from winter to summer, the corresponding water vapor amount is significantly higher in the south zone (15°-20° N, 5°-10° W) during July compared to that in February.

Figure 4 depicts the relationship between the 440 nm aerosol optical thickness and precipitable water measured by the ground sun photometer at Bidi Bahn, Burkina Faso (14° N, 2.4° W) during June-July 1996. There is clearly an anti-correlation between the aerosol optical thickness and precipitable water during this period. The ambient atmosphere is generally very moist (total precipitable water often >6 cm) in the Sahel during the month of July. As the dust plume passes by the sun-photometer site, it brings in a large amount of airborne dust as well as drier air. According to Tanre and Legrand [1991], the radiative effect of a variation of 1 g/cm^2 in precipitable water corresponds to a

variation of 1 in aerosol optical thickness. Therefore, accurate water vapor measurements are crucial in the estimation of aerosol forcing, particularly in the region south of 20° N during the summer months.

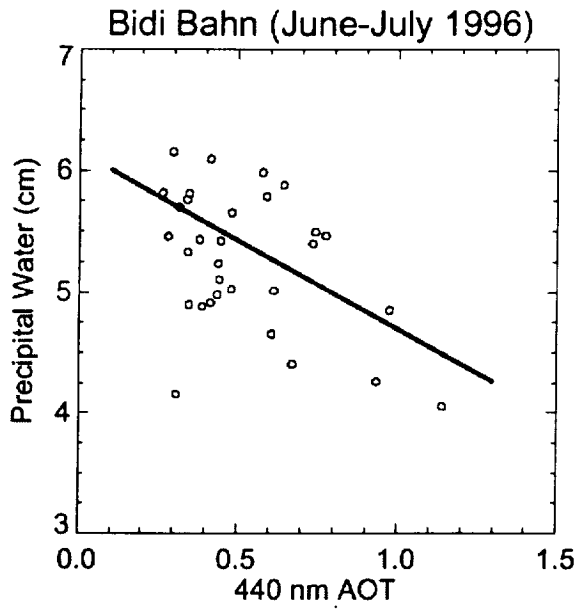

Figure 4. The relationship between the 440 nm aerosol optical thickness and precipitable water measured by the ground sun photometer at Bidi Bahn, Burkina Faso (14° N, 2.4° W) during June-July, 1996. The aerosol optical thickness appears to be anti-correlated with the precipitable water during this time period.

In contrast to the longwave response, the shortwave response is difficult to determine over land for both February and July 1985. Figure 5 shows the relationship between the ERBE TOA upward shortwave flux and TOMS aerosol index for the same region over Africa (29°-31° N; 5°-7° E) as in Figure 1 (top) for the month of July. It is apparent that the response of the TOA shortwave flux to dust loading is very weak over the desert surface for the range of solar zenith angle viewed by the NOAA-9 ERBE in 1985 (i.e., SZA ~ 20° - 30° for tropics).

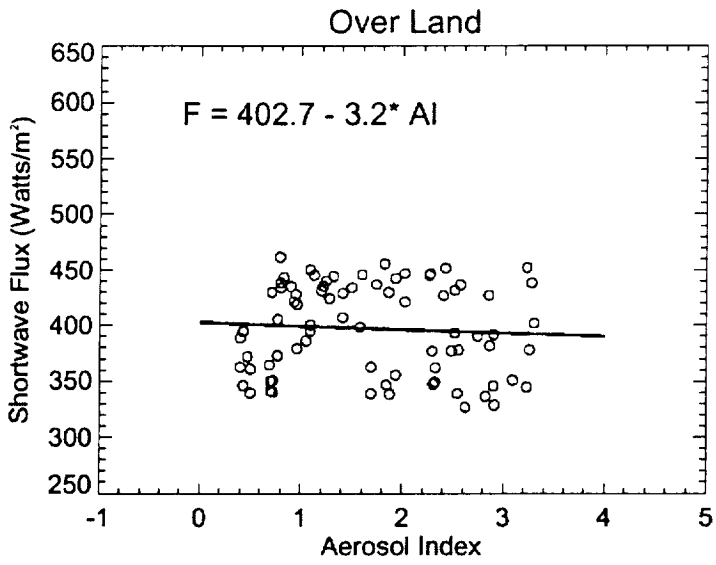

Figure 5. The relationship of the daily gridded ERBE TOA shortwave fluxes and TOMS AI measurements for the same region in Africa (29°-31° N; 5°-7° E) as in Figure 1 (top) for the month of July. The response of the TOA shortwave flux to dust loading is observed to be weak over land compared that over ocean.

3.2 TOA flux sensitivity to dust loading over ocean

Comparisons of the monthly averaged longwave and shortwave sensitivity factors of the ERBE TOA upward fluxes over ocean in February are shown in Figure 6. The values presented in the figure are the averaged sensitivity factors over the latitude band 15° -20° N as a function of longitude. The longwave sensitivity factors over the ocean are around -10 ± 2.5 W/m^2 per unit AI. Compared to the February value over land shown in Figure 2, there is clearly a difference in the response of the TOA upward longwave flux to changes in dust loading between land and ocean. This difference is most likely due to the difference in the surface temperature between land and ocean [Ackerman and Chung, 1992]. The values for the shortwave response over ocean are approximately 25 ± 6 W/m^2 per unit AI in February. The ratio of the absolute value of TOA shortwave to longwave

forcing is about 2.5 over ocean in February. This indicates that there is a net cooling effect due to the presence of mineral aerosols in the atmosphere over ocean in February.

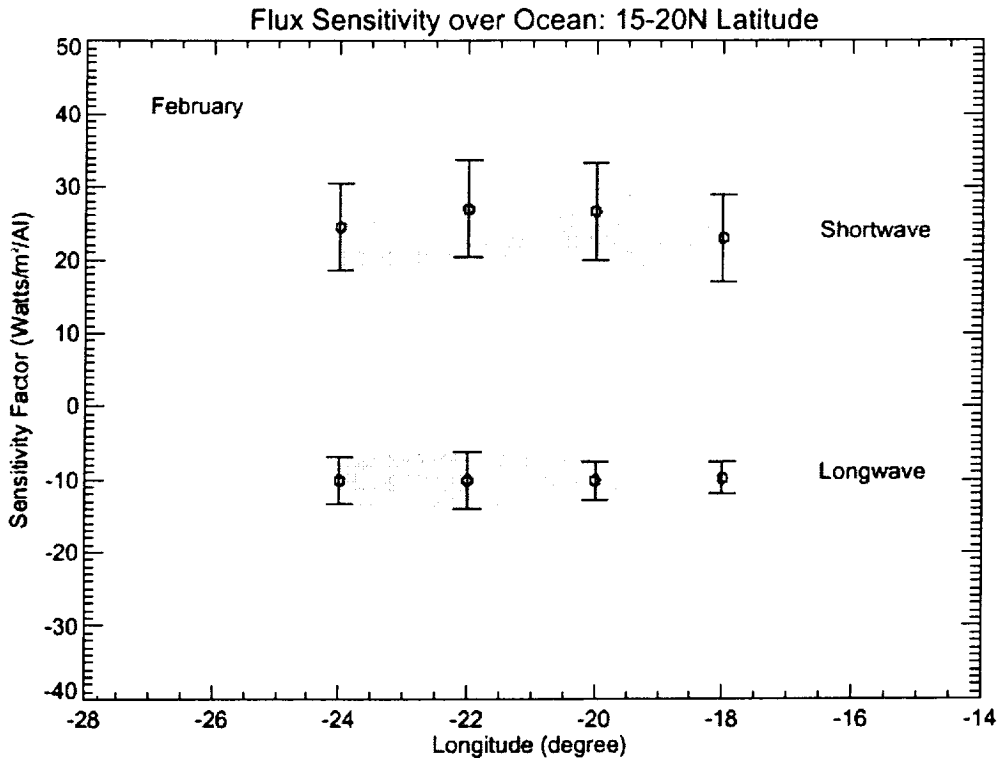

Figure 6. Comparisons of the monthly averaged longwave and shortwave sensitivity factors of the ERBE TOA upward fluxes over ocean in February. Circles represent the mean sensitivity values over 15° – 20° N latitude, and bars denote 1-σ of the sensitivity factors derived within the latitude band.

Figure 7 shows the longwave and shortwave response to dust loading over the latitude band 25°-30° N for July 1985. The general pattern of the land/ocean contrast in the longwave response to dust loading is again observed during the month of July. The values for the longwave responses in July are around -6 ± 1.5 W/m^2 per unit AI, which are smaller by as much as 30% than the values over land, as shown in Figure 3. The

values for the shortwave response over ocean are approximately 17 ± 3 W/m^2 per unit AI in July. The ratio of the absolute value of the TOA shortwave to longwave forcing is less than 3 over ocean in July. Because there are often clouds present over ocean in the region south of 20° N in the summer month, the number of the measurements made under cloud-free conditions in this region was not enough for a definite determination of the radiative forcing of mineral aerosols.

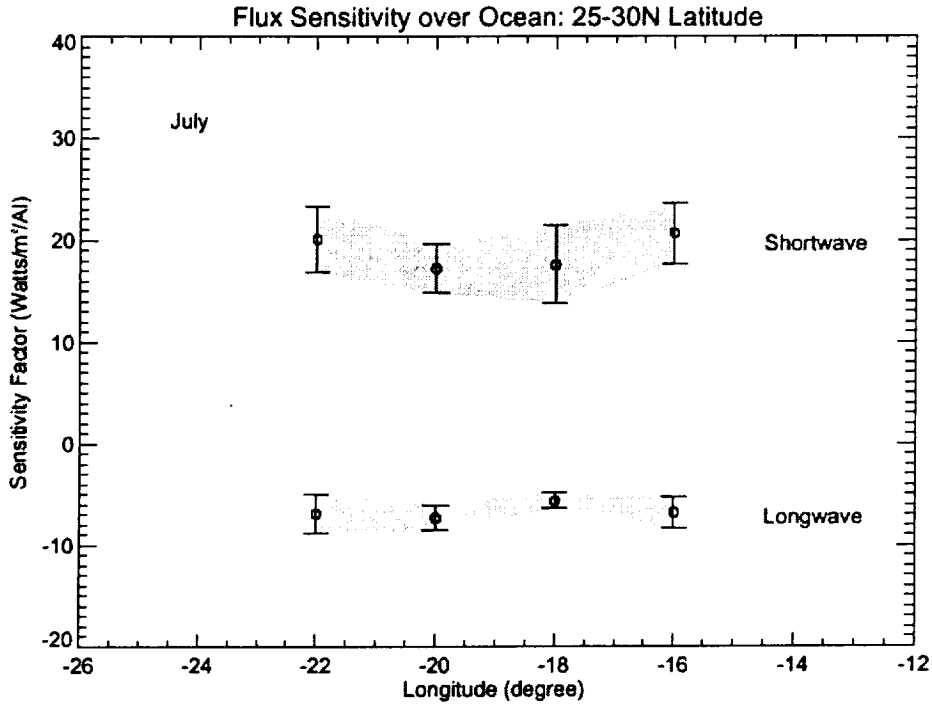

Figure 7. Similar to Figure 6, except for the latitude band 25°-30° N over ocean for July 1985.

4. Monthly averaged TOA "clear-sky" radiative forcing of Saharan dust

To obtain the monthly averaged TOA "clear-sky" radiative forcing of dust (using the method described above), we multiply the monthly mean sensitivity factor of TOA outgoing longwave and shortwave flux with the monthly mean TOMS aerosol index taken on "cloud-free" days. Plate 3 (top) and (bottom) shows the longwave and shortwave forcing of the Saharan dust for February 1985, respectively. The monthly TOA "clear-sky" longwave forcing can be as much as -15 to -30 W/m^2 over land and -10 to -15 W/m^2 over ocean. For the shortwave, the February TOA forcing is as much as 10 to 30 W/m^2 over ocean. Thus the Saharan dust results in a cooling effect on the atmospheric radiation over ocean in February by as much as 15 W/m^2 on a monthly basis.

The region south of 10° N is usually under the influence of smoke generated from biomass burning from December to March and is not shown in Plate 3. Based upon the TOMS satellite data and ground sun-photometer aerosol optical thickness data, the occurrence of the sandstorm events was quite frequent in February 1985 [Hsu et al., 1999]. There is a latitude shift from land to ocean in the maximum dust forcing that corresponds to a similar shift in the distribution of dust. This is due to the direction of the prevailing winds at this time of the year

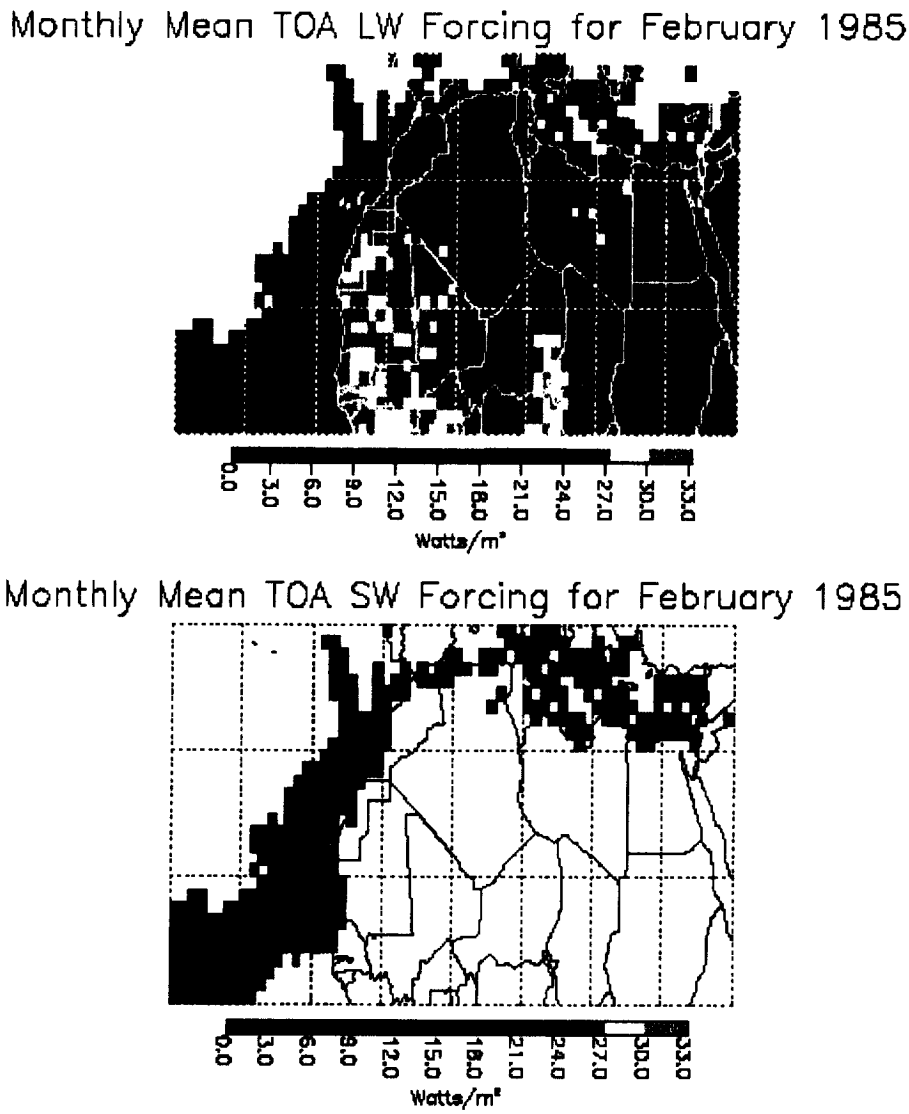

Plate 3. The monthly averaged TOA longwave (top) and shortwave (bottom) forcing of the Saharan dust for February 1985. The Saharan dust results in a monthly-average cooling effect on the atmospheric radiation over ocean during February by as much as 15 W/m^2.

The July monthly averaged TOA "clear-sky" longwave forcing is generally from -10 to -25 W/m^2 over land and -3 to -12 W/m^2 over ocean (see Plate 4). Compared to the February case, the maximum dust forcing occurs at higher latitudes near 25° N. The increased moisture in the Sahel region during July causes there to be only a small amount

of longwave forcing even in the presence of significant amounts of dust plumes in the region south of 20° N shown in Plate 4. For the shortwave, the July TOA dust forcing is as much as 40-50 W/m^2 over ocean. There is a net cooling effect of as much as 25 W/m^2 due to the presence of the Saharan dust over ocean in July.

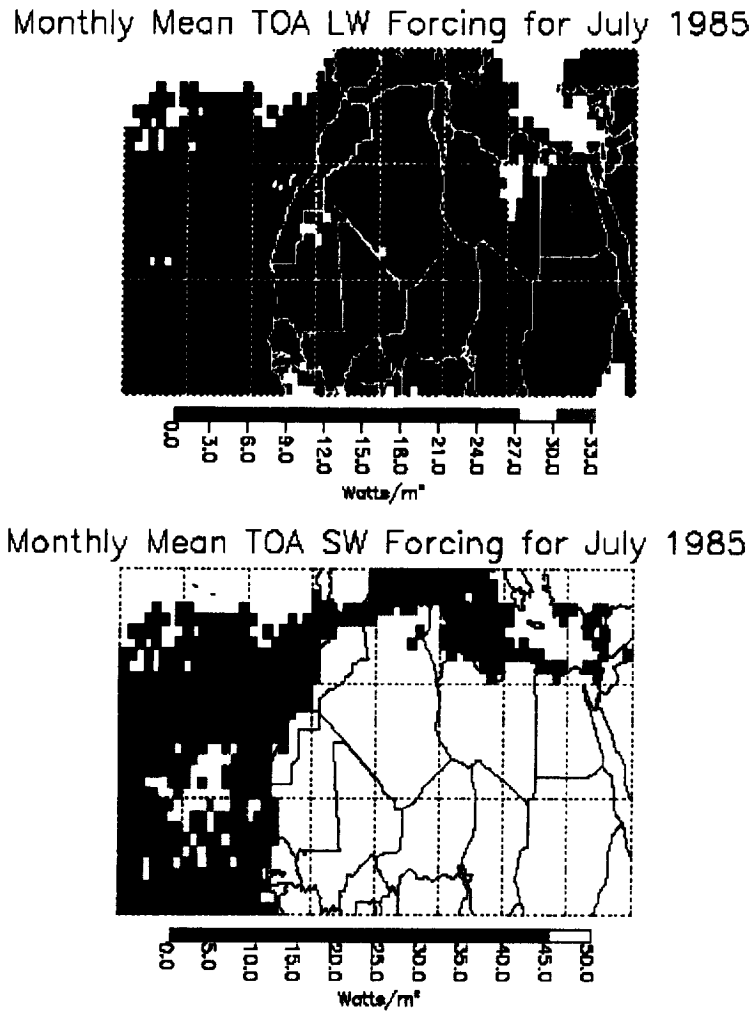

Plate 4. Similar to Plate 3, except for July 1985. There is a net cooling effect of as much as 25 W/m^2 due to the presence of the Saharan dust over ocean in July.

4.1 Effect of clouds on monthly mean dust forcing

It is important to note again that the TOA dust forcing shown in Plate 3 and 4 is for cloud-free conditions. Only satellite measurements obtained on cloudless days were included in the calculation of the monthly-mean dust forcing. Yet, the TOA mineral-dust forcing can be very sensitive to the presence or absence of clouds. Using radiative transfer simulations, Liao and Seinfeld [1998] have demonstrated that the diurnally averaged TOA longwave forcing due to mineral aerosols becomes negligible when clouds are present, while longwave forcing plays an important role in the radiative budget under clear-sky conditions. They also showed that the TOA shortwave forcing could change sign from cooling the atmosphere under clear-sky conditions to warming the atmosphere when the dust layer is above clouds.

In an attempt to investigate cloud presence on the monthly averaged longwave dust forcing, we conducted a study where we included cloudy-scene satellite measurements in the calculation of monthly averaged forcing and assumed that longwave forcing is zero for cloud/mineral aerosol mixed pixels. The results show that the monthly mean TOA longwave forcing can be reduced by 30 – 50% for July 1985. Therefore, when radiative forcing derived from satellite observations is compared with that from model simulations, the effect of clouds must be taken into account.

5. Radiative forcing of dust in terms of aerosol optical thickness

While there are nearly twenty years of aerosol index measurements taken from TOMS, extensive ground based sun-photometer measurements of AOT have only become available recently. The aerosol index has been shown to be proportional to aerosol optical thickness (AOT) using ground based sun-photometer data [Hsu et al., 1999]. We will use the results of Hsu et al. to derive the TOA radiative forcing as a funtion of AOT. These results, which are based upon the Earth-Probe TOMS data and the sun-photometer data from AERONET [Holben et al., 1998] can be summarized as follows:

Cape Verde (Ocean) (Feb.-Mar. 1997): AOT = 0.70 (± 0.10) *AI + 0.04 (± 0.14)

Cape Verde (Ocean) (May-Aug. 1997): AOT = 0.37 (± 0.04) *AI + 0.12 (± 0.07)

Bidi Bahn (Land) (Feb.-Mar. 1997): AOT = 0.85 (± 0.05) *AI - 0.18 (± 0.09)

Bidi Bahn (Land) (May-Aug. 1997): AOT = 0.30 (± 0.05) *AI + 0.25 (± 0.11)

Based upon these relationships, and the aerosol wavelength adjustment constant between Nimbus-7 and Earth-Probe TOMS [Hsu et al., 1999], we converted the dust forcing per unit AI shown in the previous section into per unit AOT for the sun-photometer sites. Figure 8 shows the TOA longwave and shortwave forcing for both land and water for two different months. The latitude for the land and ocean case is 10° – 20° N for February and 25° – 30° N for July. The TOA longwave forcing is approximately –32 W/m^2/AOT over land in February and -36 W/m^2/AOT over land in July. The TOA

longwave forcing over ocean is about -20 W/m^2/AOT in February and -24 W/m^2/AOT in July. The shortwave forcing over ocean is roughly 52 W/m^2/AOT in February and 60 W/m^2/AOT in July. The solar zenith angles corresponding to these ERBE measurements are approximately 20° – 30°.

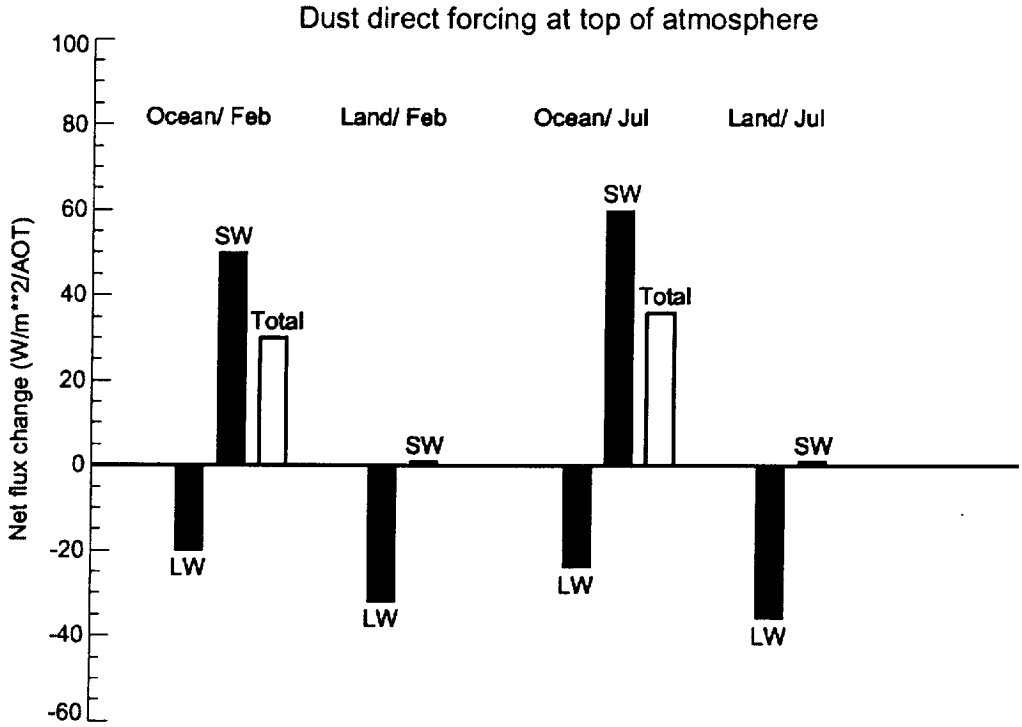

Figure 8. Summary of the estimated TOA longwave and shortwave direct forcing of dust per unit AOT over land and ocean surfaces for February and July

6. Theoretical simulations of TOA direct forcing of airborne dust

These observed results can be compared with radiative calculations using a 1-dimensional version of the GEOS-2 GCM radiative transfer model [Chou, 1992; Chou and Suarez, 1994]. To calculate the TOA longwave and shortwave fluxes, we first choose vertical profiles for temperature, moisture and cloud fraction on 8 August 1988 at 24° N, 25° W (ocean) and 24° N, 12° W (land) from the GEOS-2 assimilation.

A second calculation uses a modified version of the radiative transfer model that accounts for the spectral dependence in aerosol optical depth, single scattering albedo and asymmetry factor. These profiles are calculated from the conditions occuring on 8 August using four dust particle size ranges, simulated by a dust transport model (Paul Ginoux, personal communication) and optical parameters for Sarahan dust based on Mie scattering theory. The dust optical parameters, which are dependent on wavelength and particle size, were provided by A. Lacis, and are the same values used in recent radiative calculations by Tegen and Lacis [1996].

The differences between the clean and dusty atmosphere TOA upward flux (defined in the same fashion as in Section 3) are shown in Figure 9 for the long and short wave bands. The ERBE observations were made at approximately 2:30 p.m. local equator crossing time, which is close to 15 GMT for the profile locations. The change in TOA shortwave flux over ocean at 15 GMT (long dashed) is not quite linear with AOT (as shown in the left panel). There is a 75 W/m^2 increase in TOA shortwave flux for the first AOT and less of a reduction for each additional AOT. This is consistent with the observed 60 W/m^2 increase in SW over ocean in Figure 8. The TOA shortwave flux also increases with increasing AOT at all zenith angles.

However, over land (as shown in the right panel) the situation is more complex. At low zenith angles, absorption by dust reduces the TOA outgoing shortwave radiation (dotted line). At high zenith angles enough of the radiation that would have been absorbed at noon is now scattered back to space and the TOA upward shortwave flux actually increases (solid and dotted-dash lines). The TOA shortwave flux over land is not

sensitive to atmospheric dust loading at 15 GMT (long-dash line), which explains the poor relationship between the ERBE observed TOA shortwave flux and AI over land.

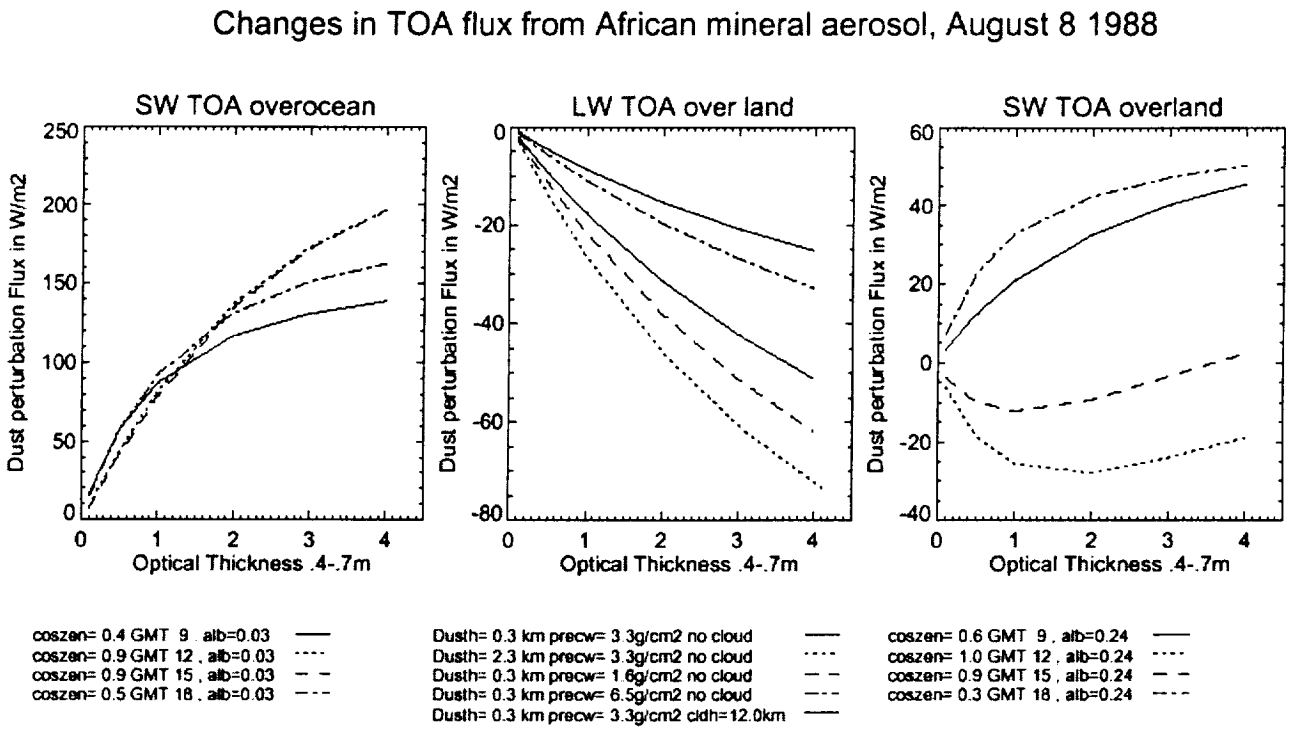

Figure 9. The model-calculated differences between the clean and dusty atmosphere TOA upward longwave and shortwave flux (defined in the same fashion as in Section 3). The ERBE observations were made at approximately 2:30 p.m. local equator crossing time, which is close to 15 GMT for the profile locations. (Left) The response of the TOA upward shortwave flux to changes in AOT over ocean as a fuction of solar zenith angle; (Right) Similar to (the left), except for the land condition; (Center) The sensitivity of the model-calculated TOA instantaneous longwave dust forcing to dust layer height, moisture content, and the presence of clouds.

The center panel shows the sensitivity of the TOA longwave radiation over land to elevation of the dust layer, the moisture content and the presence of clouds. The solid line is the standard profile (assuming dust height = 0.3 km, precipitable water = 3.3 g/cm^2, and no cloud), and it shows a decrease of about 17 W/m^2 in TOA longwave flux per unit AOT. This is significantly less than the observed 32 W/m^2 per unit AOT shown in Figure 8. However, the model-calculated response of the longwave radiation changes significantly with changes to the input parameters. For example, the decrease in the longwave radiation becomes 22 W/m^2 per unit AOT when the ambient precipitable water is decreased by 50 % (long-dash line). Also, as the dust height was elevated from 0.3 km to 2.3 km, the TOA longwave flux decreases by 27 W/m^2 per unit AOT under the same moisture condition of 3.3 g/cm^2. Finally, placing a cloud at 12 km (bold curve) significantly reduces the sensitivity of LW TOA to dust loading which is consistent with the results of Liao and Seinfeld (1998).

7. Conclusions

In this study, we derive the TOA direct forcing of airborne Saharan dust using satellite data from TOMS and ERBE. Our results clearly indicate that the signature of the mineral aerosols can be traced in the longwave and shortwave fluxes at the top of the atmosphere. For "cloud-free and dry" conditions, the ratio of the shortwave to longwave forcing due to Saharan mineral dust is found to be roughly 2 to 3, but opposite in sign, over ocean for both February and July. It indicates a net cooling effect in the atmosphere over ocean. However, over land and when the solar zenith angle is about $20^{\circ} - 30^{\circ}$, the response of the ERBE shortwave flux to changes in dust loading seems to be weak and noisy, while the observations show a strong longwave forcing in the same region. The results of the TOA direct forcing due to airborne Saharan dust on the daily and monthly basis are summarized in Table 1.

Table 1. Summary of the daily and monthly TOA direct radiative forcing of airborne Saharan dust for both longwave and shortwave fluxes (in units of W/m^2)

	Daily (W/m^2)		Monthly (W/m^2)	
	SW	**LW**	**SW**	**LW**
Land		-10 ~ -50		-15 ~ -30 (Feb) -10 ~ -25 (Jul)
Ocean	20 ~ 100	-5 ~ -30	10 ~ 30 (Feb) 40 ~ 50 (Jul)	-10 ~ -15 (Feb) -3 ~ -12 (Jul)

For "moist" conditions, such as in the Sahel during summer time, we found that there is a very weak response of the longwave radiation to the passage of the Saharan dust layer. This may be due to the fact that the effect of mineral aerosol nearly cancels out with the water vapor effect on the longwave radiation, as a result of the anti-

correlation found between the precipitable water and aerosol optical thickness the Sahel region.

Since the Nimbus-7 TOMS data were taken near noon and the NOAA-9 ERBE measurements were made at around 2:30 p.m., this time difference could potentially introduce uncertainties in our results. To investigate uncertainties due to this time difference, we conducted similar analyses using the Nimbus-7 TOMS measurements and ERBE data from the ERBS satellite taken during July 30 – August 6 1988. The time difference between measurements from these two satellites during this time was less than 30 minutes. We found that the responses of the longwave and shortwave fluxes to dust loading derived from this experiment are similar to those determined above. This is probably due to the fact that although the temporal variation in clouds is large, the amounts of airborne dust associated with large-scale dust storms do not change significantly between noon and early afternoon (on a 1^{o} x 1^{o} grid average scale). Other factors, which could potentially impact the results of our analyses, include the uncertainty associated with the effects of random noise and natural atmospheric variability. However, they are expected to be small since we use a large amount of satellite measurements made over a vast area during several months (February to July).

The effects of tropospheric aerosols and water vapor in climate forcing are complex in the real atmosphere. Simulations by GCM models depend greatly on the input aerosol properties, and will not be well determined in the absence of simultaneously measured aerosol and water-vapor data. Based upon in-situ measurements taken in different regions of the world, there is a very wide range of the optical properties of mineral aerosols [Sokolik and Toon, 1999]. Our results provide useful constraints on the

model assumptions of these dust aerosol properties and further reduce the uncertainty in determining the aerosol effect on radiation budget for regional and global climate models.

Acknowledgment. The authors would like to thank J. Susskind and P. Piraino for providing the HIRS2 cloud and water vapor data, the NASA/Langley Distributed Active Archive Center (DAAC) for providing the ERBE data. The radiative transfer code was kindly provided by Ming-Dah Chou.

References

Ackman, S. A., and H. Chung, Radiative effects of airborne dust on regional energy budgets at the top of the atmosphere, *J. Appl. Meterol.*, 31, 223-233, 1992.

Barkstrom, B. R., E. F. Harrison, G. Smith, R. Green, J. Kebler, R. Cess, and the ERBE science team, Earth Radiation Budget Experiment (ERBE) archival and April 1985 results, *Bull. Amer. Meteor. Soc.*, 70, 1254-1262, 1989.

Chou, M., A solar radiation model for use in climate studies, *J. Atmos. Sci.*, 49, 762-772, 1992.

Chou, M., and M. J. Suarez, An efficient thermal infrared radiation parameterization for use in general circulation models, In: technical report series on global modeling and data assimilation, vol. 3, edited by M. J. Suarez, NASA memorandum 104606, 1994.

Christopher, S. A., D. A. Kliche, J. Chou, and R. M. Welch, First estimates of the radiative forcing of aerosols generated from biomass burning using satellite data, *J. Geophys. Res.*, 101, 21265 – 21273, 1996.

Hansen, J. E., and A. A. Lacis, Sun and dust versus greenhouse gases: An assessment of their relative roles in global climate change, *Nature*, 346, 713-719, 1990.

Herman, J. R., P. K. Bhartia, O. Torres, N. C. Hsu, C. J. Seftor, and E. Celarier, Global distribution of UV-absorbing aerosols from Nimbus-7/TOMS data, *J. Geophys. Res.*, 102, 16911-16922, 1997.

Holben, B. N., et al., AERONET- a federated instrument network and data archive for aerosol characterization, *Remote Sens. Environ.*, **66**, 1-16, 1998.

Houghton, J. T., G. J. Jenkins, and J. J. Ephraums, eds, Climate change: The IPCC Scientific Assessment, Cambridge Univ. Press, Cambridge, 362pp., 1990.

Hsu, N. C., J. R. Herman, P. K. Bhartia, C. J. Seftor, O. Torres, A. M. Thompson, J. F. Gleason, T. F. Eck, and B. N. Holben, Detection of biomass burning smoke from TOMS measurements, *Geophy. Res. Lett.*, 23, 745-748, 1996.

Hsu, N. C., J. R. Herman, O. Torres, B. N. Holben, D. Tanre, T. F. Eck, A. Smirnov, B. Chatenet, and F. Lavenu, Comparisons of the TOMS aerosol index with sun-photometer aerosol optical thickness: results and applications, *J. Geophys. Res.*, 104, 6269-6279, 1999.

IPCC, Radiative forcing. In: Climate Change 1994- Radiative forcing of climate change and an evaluation of the IPCC 1992 emission scenarios, ed. J. T. Houghton, L. G. M. Filho, J. P. Bruce, H. Lee, B. T. Callander, E. F. Hailes, N. Harris, and K. Maskell. Cambridge: Cambridge Univ. Press, 352pp., 1994.

Liao, H., and J. H. Seinfeld, Radiative forcing by mineral dust aerosols: sensitity to key variables, *J. Geophys. Res.*, 103, 31637-31645, 1998.

Penner, J. E., R. J. Charlson, J. M. Hales, N. Laulainen, R. Leifer, T. Novakov, J. Ogren, L. F. Radke, S. E. Schwartz, and L. Travis, Quantifying and minimizing uncertainty of climate forcing by anthropogenic aerosols, *Bull. Am. Meteorol. Soc.*, 75, 375-400, 1994.

Seftor, C. J., N. C. Hsu, J. R. Herman, P. K. Bhartia, O. Torres, W. Rose, D. Schneider, and N. Krotkov, Detection of volcanic ash clouds from Nimbus-7/TOMS, *J. Geophys. Res.*, 102, 16749-16759, 1997.

Smith, G. L., R. N. Green, E. Raschke, L. B. Avis, J. T. Suttles, B. A. Wielicki, and R. Davies, Inversion methods for satellite studies of the earth's radiation budget: Development of algorithms for the ERBE mission, *Rev. Geophys.*, 24, 407-421, 1986.

Sokolik, I. N., O. B. Toon, and R. W. Bergstrom, Modeling the radiative characteristics of airborne mineral aerosols at infrared wavelengths, *J. Geophys. Res.*, 103, 8813-8826, 1998.

Sokolik, I. N., and O. B. Toon, Incorporation of mineralogical composition into models of the radiative properties of mineral aerosol from UV to IR wavelengths, *J. Geophys. Res.*, 104, 9423-9444, 1999.

Susskind, J., P. Piraino, L. Rokke, L. Iredell, and A. Mehta, Characteristics of the TOVS Pathfinder Path A dataset, *Bull. Am. Meteo. Soc.*, 78, No. 7, 1449-1472, 1997.

Suttles, J. T., B. A. Wielicki, and S. Vemury, Top-of-atmosphere radiative fluxes: validation of ERBE scanner inversion algorithm using Nimbus-7 ERB data, *J. Appl. Meteor.*, 31, 784-796, 1991.

Tanre, D., and M. Legrand, On the satellite retrieval of Saharan dust optical thickness over land: two different approaches, *J. Geophys. Res.*, 96, 5221-5227, 1991.

Tanre, D., E. Vermote, B. N. Holben, and Y. J. Kaufman, Satellite aerosol retrieval over land surfaces using the structure functions, In: IGARSS '92, Proceedings of the 12th annual international geoscience and remote sensing symposium, 2, 1474-1477, 1992.

Tegen, I., A. A. Lacis, and I. Fung, The influence on climate forcing of mineral aerosols from disturbed soils, *Nature*, 380, 419-422, 1996.

Tegen, I., and A. A. Lacis, Modeling of particle size distribution and its influence on the radiative properties of mineral dust aerosol, *J. Geophys. Res.*, 101, 19237-19244, 1996.

Torres, O., P. K. Bhartia, J. R. Herman, Z. Ahmad, and J. Gleason, Derivation of aerosol properties from satellite measurements of backscattered ultraviolet radiation. Theoretical basis, *J. Geophys. Res.*, 103, 17099-17110, 1998.

Figure Captions

Plate 1. (Top) Maps of the top-of-atmosphere longwave upwelling fluxes observed by the NOAA-9 ERBE scanner in February 1985. The corresponding daily composites of aerosol index and reflectivity derived from TOMS are depicted in Plate 1 (Bottom). Clouds are usually associated with relatively higher reflectivity and are represented by the gray color shown in the bottom left color bar.

Plate 2. (Top) Similar to Plate 1 (top), except for the top-of-atmosphere shortwave upwelling fluxes. (Bottom) The TOMS aerosol index and reflectivity represented in the similar way as in Plate 1 (bottom). The areas included in these images are centered over the Atlantic just west of Africa.

Figure 1. (Top) The relationship of the daily gridded ERBE TOA longwave fluxes and TOMS AI measurements for a 2^{o} x 2^{o} box in Africa (29^{o}-31^{o} N; 5^{o}-7^{o} E) for the month of July. The linear-regression fit to these data is represented by the solid line. (Bottom) The relationship of the daily gridded ERBE TOA shortwave fluxes and the TOMS AI measurements for a 2^{o} x 2^{o} box in the Atlantic (25^{o}-27^{o} N; 19^{o}-21^{o} W) for the month of July.

Figure 2. Values of the longwave sensitivity factor derived over land as a function of longitude. The sensitivity factors derived for each 1^{o} x 1^{o} grid box were averaged over a 5^{o} latitude band for 15^{o} – 20^{o} N during February (top), and 29^{o} – 33^{o} N during July (bottom). Circles represent the mean values and bars denote 1-σ of the sensitivity factors derived within the latitude band.

Figure 3. The seasonal variations (February to July 1985) of total precipitable water from HIRS2 measurements for the south zone (15^{o}-20^{o} N, 5^{o}-10^{o} W) (+ symbols) and the north zone (27^{o}-32^{o} N, 5^{o}-10^{o} W) (* symbols). Because the position of the ITCZ moves northward from winter to summer, the corresponding water vapor amount is significantly higher in the south zone (15^{o}-20^{o} N, 5^{o}-10^{o} W) during July compared to that in February.

Figure 4. The relationship between the 440 nm aerosol optical thickness and precipitable water measured by the ground sun photometer at Bidi Bahn, Burkina Faso (14° N, 2.4° W) during June-July, 1996. The aerosol optical thickness appears to be anti-correlated with the precipitable water during this time period.

Figure 5. The relationship of the daily gridded ERBE TOA shortwave fluxes and TOMS AI measurements for the same region in Africa (29°-31° N; 5°-7° E) as in Figure 1 (top) for the month of July. The response of the TOA shortwave flux to dust loading is observed to be weak over land compared that over ocean.

Figure 6. Comparisons of the monthly averaged longwave and shortwave sensitivity factors of the ERBE TOA upward fluxes over ocean in February. Circles represent the mean sensitivity values over 15° – 20° N latitude, and bars denote 1-σ of the sensitivity factors derived within the latitude band.

Figure 7. Similar to Figure 6, except for the latitude band 25°-30° N over ocean for July 1985.

Plate 3. The monthly averaged TOA longwave (top) and shortwave (bottom) forcing of the Saharan dust for February 1985. The Saharan dust results in a monthly-average cooling effect on the atmospheric radiation over ocean during February by as much as 15 W/m^2.

Plate 4. Similar to Plate 3, except for July 1985. There is a net cooling effect of as much as 25 W/m^2 due to the presence of the Saharan dust over ocean in July.

Figure 8. Summary of the estimated TOA longwave and shortwave direct forcing of dust per unit AOT over land and ocean surfaces for February and July.

Figure 9. The model-calculated differences between the clean and dusty atmosphere TOA upward longwave and shortwave flux (defined in the same fashion as in Section 3). The ERBE observations were made at approximately 2:30 p.m. local equator crossing time, which is close to 15

GMT for the profile locations. (Left) The response of the TOA upward shortwave flux to changes in AOT over ocean as a fuction of solar zenith angle; (Right) Similar to (the left), except for the land condition; (Center) The sensitivity of the model-calculated TOA instantaneous longwave dust forcing to dust layer height, moisture content, and the presence of clouds.

Table 1. Summary of the daily and monthly TOA direct radiative forcing of airborne Saharan dust for both longwave and shortwave fluxes (in units of W/m^2)

	Daily (W/m^2)		Monthly (W/m^2)	
	SW	**LW**	**SW**	**LW**
Land		-10 ~ -50		-15 ~ -30 (Feb) -10 ~ -25 (Jul)
Ocean	20 ~ 100	-5 ~ -30	10 ~ 30 (Feb) 40 ~ 50 (Jul)	-10 ~ -15 (Feb) -3 ~ -12 (Jul)